Large Area Imaging Detector for Long-Range, Passive Detection of Fissile Material

Klaus P. Ziock, William W. Craig, Lorenzo Fabris, Richard C. Lanza, Shawn Gallagher, Berthold K. P. Horn, and Norm W. Madden

***Abstract*—Recent events highlight the increased risk of a terrorist attack using either a nuclear or a radiological weapon. One of the key needs to counter such a threat is long-range detection of nuclear material. Theoretically, gamma-ray emissions from such material should allow passive detection to distances greater than 100 m. However, detection at this range has long been thought impractical due to spatially fluctuating levels of natural background radiation. These fluctuations are the major source of uncertainty in detection and mean that sensitivity cannot be increased simply by increasing detector size. Recent work has shown that this problem can be overcome through the use of imaging techniques. In this paper we describe the background problems, the advantages of imaging and the construction of a prototype, large-area (0.57 m^2) gamma-ray imager to detect nuclear materials at distances of $\sim$ 100 m.**

***Index Terms*—Coded aperture imager, gamma-ray detectors, gamma-ray imagers, radiation source search.**

I. Introduction

NUCLEAR material cannot be detected at long range using traditional methods because its presence is masked by background radiation of unknown and spatially varying intensity [1]. Adding imaging to detection allows one to estimate the local background, making it possible to detect spatially localized radioactive sources from considerable distances.

To understand why imaging gives an order of magnitude or so improvement in performance in a passive search scenario, one must understand the limitations imposed by the use of an omni-directional, gamma-ray detector. We start by defining the count rate observed in our detector at a random location in the region to be searched as the background, B counts/m^2/keV/sec. If we then use the same detector and move it around our search area, we find that B varies by as much as a factor of five from one place to another [2]–[4]. Suppose a source of strength, S counts/keV/sec is to be found. To minimize the search time, we try to detect the source from as far away as possible. The source is "detected" when the signal from it exceeds the noise by some fixed ratio—e.g., when the signal is five times as strong as the noise.

Manuscript received October 29, 2003; revised July 8, 2003. Portions of this work were performed under the auspices of the U.S. Department of Energy by University of California, Lawrence Livermore National Laboratory under Contract W-7405-Eng-48.

K. P. Ziock, W. W. Craig, L. Fabris, and N. W. Madden are with Lawrence Livermore National Laboratory, Livermore, CA 94550 USA (e-mail: ziock1@llnl.gov).

R. C. Lanza, S. Gallagher, and B. K. P. Horn are with the Massachusetts Institute of Technology, Cambridge, MA 02139 USA (e-mail: lanza@mit.edu; bkph@ai.mit.edu).

Digital Object Identifier 10.1109/TNS.2004.836117

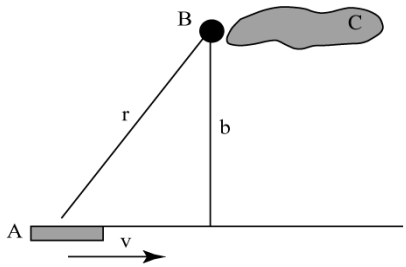

Fig. 1. Geometry used in simulations. The detector (A) tracks past a source (B) at a distance of closest approach (b) with a velocity (v). For the imaging simulations, the mask is at the front of the top edge of the imager and detector is at the bottom. The light gray region (C) to the right of the source indicates an area that doubles the normal background in the detector.

If the background were a constant, we would write the signal-to-noise ratio (SNR) as

$$\mathrm{SNR} = \frac{s(r)}{\sqrt{s(r)+B}} = \frac{\frac{SA\varepsilon t}{4\pi r^2}}{\sqrt{\frac{SA\varepsilon t}{4\pi r^2} + Ab(r)\varepsilon t}} \propto \sqrt{At} \qquad (1)$$

where A is the detector area, t is the measurement dwell time, $s(r)$ is the signal, $b(r)$ is the local background rate, and ε is the detector efficiency. We find that longer dwell times and larger detectors give a better SNR and, hence, improve the search range. Unfortunately, this does not apply to the detection of weak emissions from nuclear materials in the field.

Equation (1) assumes that we are limited by counting statistics (i.e., we know the background, so the standard deviation of our measurement is the square root of the total number of counts detected). But in practice, we do not know the spatially varying background and hence the appropriate expression is:

$$\mathrm{SNR} = \frac{s(r)}{B} = \frac{\frac{SA\varepsilon t}{4\pi r^2}}{Ab(r)\varepsilon t} \propto \frac{At}{At} = \text{Constant} \qquad (2)$$

In this case, the SNR is independent of both A and t. As a result, neither a larger detector, nor a longer dwell time can improve the SNR.

This situation is shown by a simulation using the source detector geometry presented in Fig. 1. The counts expected as the detector tracks past a one millicurie ^{137}Cs source at a fixed velocity are calculated for a given detector area. We assume a background rate of approximately one count per square centimeter per second that doubles in the region C. In the top panel of Fig. 2 we show the counts reaching the detector for different distances of closest approach (which occurs at $x = 0$) without including counting statistics. The broad increase in counts centered at $\sim x = 25$ m represents the factor of two increase in the background. As can be seen, once the detector is 20 m from

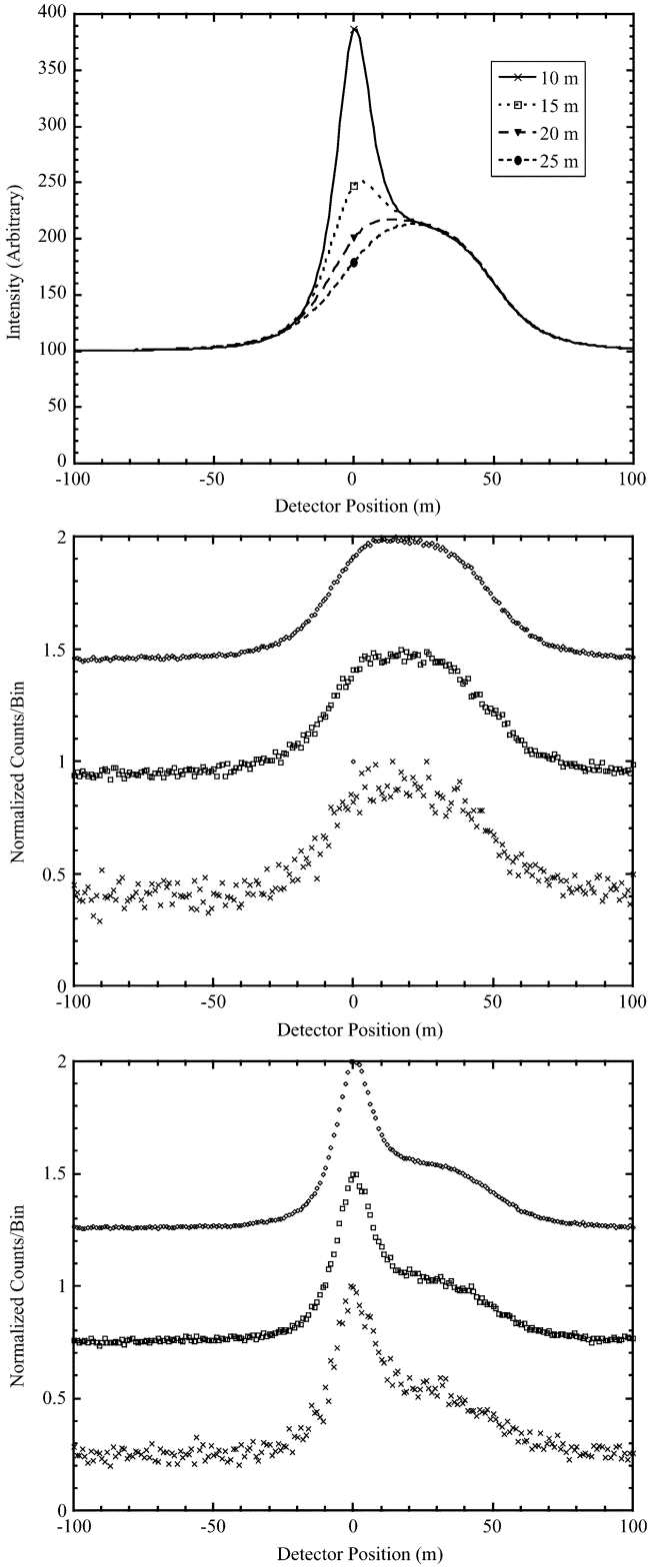

Fig. 2. Response of a detector passing by a fixed point source. The top plot shows the noiseless response for different distances of closest approach. The middle plot shows the response for detectors of 100, 1 000, and 10 000 cm^2 area (bottom to top trace, offset by 0.5 for clarity) passing the source at a distance of closest approach of 10 m and includes counting statistics noise. The bottom plot shows the response for detectors of 100, 1 000, and 10 000 cm^2 area (bottom to top trace, offset by 0.5 for clarity) passing the source at a distance of closest approach of 20 m and includes counting statistics noise. While a larger detector improves the counting statistics, it clearly does not improve the range at which a source can be detected.

the source, the source contribution cannot be distinguished from the broad background bump. In the middle and bottom panels of Fig. 2, we show the (normalized) results as expected for detectors of effective areas of 100 cm^2, 1 000 cm^2, and 10 000 cm^2 but now include counting statistics. The middle panel is for a distance of closest approach of 10 m while the bottom panel is for 20 m. It is clear that without prior knowledge of the shape of the background bump, the source is not visible in the bottom panel; even as the detector area is increased by two orders of magnitude.

One solution to this problem is to apply imaging to separate background and source gamma-rays. However, at the gamma-ray energies emitted by most sources of interest ($\sim$100 keV–3 MeV) the only direct imaging technique is the very inefficient pinhole camera. Although indirect imaging techniques such as coded apertures, [5] rotation modulation collimators [6], or fourier transform cameras [7] can increase the efficiency of an imager, they do not provide much information on the direction of origin a single gamma-ray. These devices image in a statistical fashion and on first look cannot improve on the signal-to-noise ratio of an uncollimated detector, i.e., by blocking photons one cannot improve on the detectability of a source, one can only improve the localizability of a point source over that obtained with a pinhole camera.

However, in our problem, imaging allows us to use the prior knowledge that we are only interested in point sources. We make use of this information by looking for isolated sources that produce a slightly enhanced flux in a limited area of the image (i.e., only a few pixels are affected by the photon flux from the source). The local, slowly-varying, background can be determined from the neighboring pixels in the image. This means we know the background and can use the SNR expression given by (1) instead of the one given by (2). For a very large detector, of the sort we are building, the background rate can be as high as 1 000 cnts/s so that the improvement in SNR is $\sim$30.

This situation is shown in Fig. 3 where we revisit the problem with the geometry of Fig. 1 but use the imaging properties of a one-dimensional, coded-aperture imager. As the imager tracks past the source, it collects a series of "snap-shots." These images have noise added to each pixel commensurate with the coded aperture nature of the images, i.e., proportional to the square root of the total counts in the detector [8]. The (noisy) images are added together to make a single image for the full track of the instrument past the source. The figure shows the normalized traces obtained by different sized detectors at different distances of closest approach. The top trace shows a successful detection of the source at 50 m using a large detector. Based on these results we are building the large imager described below.

II. Large Imager Design

Our large-area imager is based on a one-dimensional, coded aperture design that uses existing, cubic, $10 \times 10 \times 10$ cm^3 NaI detectors. A photograph of the imager with one row of the detectors installed is shown in Fig. 4. The coded aperture mask is based on a 19-element, one-dimensional, uniformly redundant array (URA) pattern [9]. It is constructed of linotype metal (an alloy with 85% Pb, 11% Sb, 3% Sn, and 1% other materials)

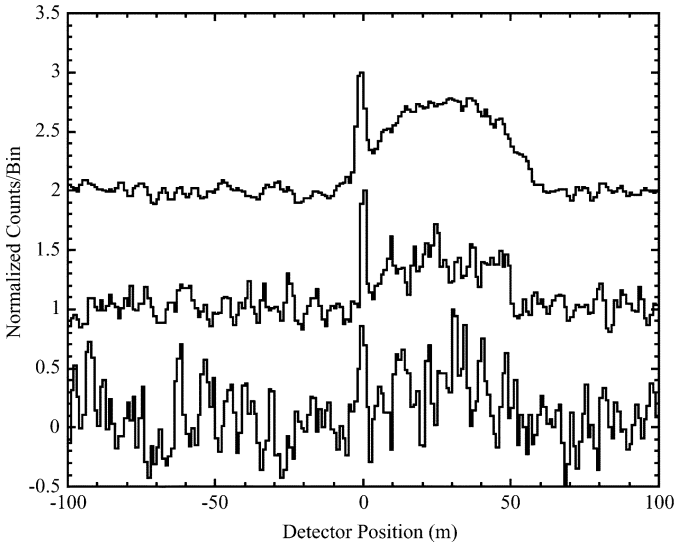

Fig. 3. Normalized response of an imaging detector passing past the source/background configuration of Fig. 1. Bottom to top trace are for 100 cm^2 detector at 30 m closest approach, 1 000 cm^2 detector at 30 m closest approach and a 10 000 cm^2 detector at 50 m closest approach. (The traces are offset by one for clarity.) Larger imaging detectors clearly help.

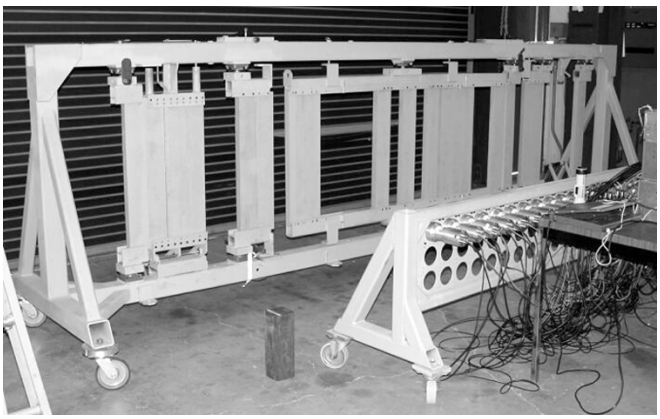

Fig. 4. Picture of the imager showing the mask and the detector array. Only the top row of the 19 × 3 detector array is installed.

4-cm thick with a 10.8-cm pitch imposed by the extant detectors. One-dimensional imaging was selected for ease of implementation and the proposed suburban, light-urban search application for the instrument. Long-range search in dense urban areas is extremely difficult due to the shielding effects of concrete floors in high-rise buildings of more than a few floors. Further motivation and design details are presented below.

A. Monte Carlo Simulations

A Monte Carlo code was developed to optimize the imager response and develop data handling algorithms. The code was designed to simulate the counts viewed by the system as it tracks past a source. It includes such effects as atmospheric attenuation, finite mask thickness, number of mask elements, detector velocity, and variable collimation. The location of the source along the track, the distance of closest approach and the source strength are all variable quantities so that different problems can

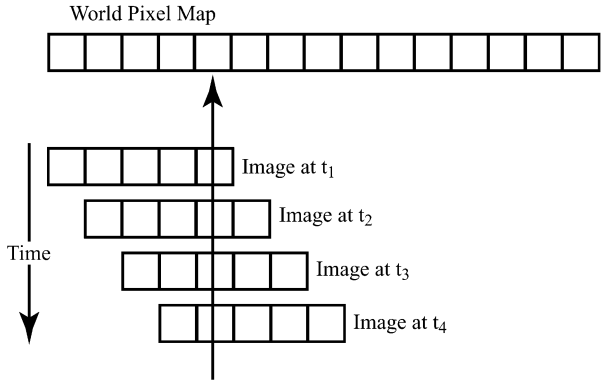

Fig. 5. A world image is created by summing the sequential images made by the imager as it moves with time.

be run. In addition, the strength of the background is a free parameter that includes a constant and/or a sinusoidally varying fluence. The sinusoidal variation is by position.

1) Simulation Implementation: In the code, the position of the imager is stepped in one millisecond increments. During each step, the flux from a point source at a definable distance and location of closest approach is calculated. The calculation is based on the source strength, the detector solid angle at the current location and atmospheric attenuation. The area of the detector is fixed (generally) at one square meter and is assumed to have unit quantum efficiency. A Poisson generator [10] is used to select the number of counts incident on the detector array during the step. These are randomly distributed across the array face which uses individual pixels of 10-cm width. A variable pixel spacing would help compensate for distance effects, but this was not possible with our detector hardware. Based on the event location and the geometry to the source, the mask elements that the photon traverses at the front and back of the mask are calculated. If either of these is opaque, then the event is rejected. This approach is the simplest way to simulate the effects of finite mask thickness. In addition, slat collimators of selectable length between the individual pixels are used to impose a collimation function.

Note that the collimator and mask material is assumed to be completely opaque to the radiation. This neglects radiation that is transmitted or scattered by the material. The first order effect of such radiation is to add to the unmodulated background in the detector which does not affect the imaging. Second order effects, where mask edges transmit slightly more radiation, are assumed negligible and will be dealt with in the future. If an event survives all of these obstacles, then it is recorded in the appropriate detector pixel.

As the imager is moved through the simulated world, its location is compared to a predefined array of world pixels. If the imager reaches the edge of one of these pixels, then an image is created from the detector array and the image is added to the world image (See Fig. 5). In this way a map of counts versus location is generated.

The world map generation described above is really only correct for sources at a single distance from the imager. Since we search for sources at an unknown distance, we actually use the same data to create 10 separate world maps, each 10-meters

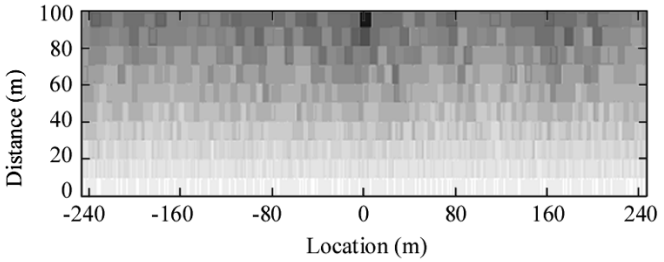

Fig. 6. Sample scan past a 1 mCi ^{137}Cs source at 95 m distance of closest approach, at a speed of 40 km/h for a 0.57 m^2 detector area and a background rate of 500 counts/sec/m^2. The distance from the imager track increases up the image in 10 m steps. The source is clearly visible at the top of the image.

deep, centered at distances of $5, 15, 25, \ldots, 95$ m from the mask face. This is done by simultaneously collecting the gamma-ray hits into 10 separate detector arrays, one associated with each of 10 values of closest approach. All events are added to each of these detector arrays. As the imager position is incremented, a check is made to see if the detector location equals or exceeds the lateral edge of one of the corresponding ten fixed world-pixel maps. These maps are correlated with the world-pixel size for each distance bin determined from the angular resolution of the imager. The resolution is given by the mask pixel size divided by the mask-to-detector spacing (focal length) times the average distance of closest approach. If a bin edge is exceeded, then the data in the detector array for that distance is used to generate an image and the image is added to the appropriate world pixel map. The virtual detector array tuned for that distance is zeroed and the system continues. Note that the algorithm uses the same photon set for all 10 maps, it is just binned appropriate to the relative motion of world pixels at that distance.

Sample results from the simulations are shown in Fig. 6 where the images of a scan at 40 km/h past a one millicurie ^{137}Cs source with a background rate of 500 cnts/m^2/sec are shown. The figure shows the ten world maps generated in the course of the simulation. Each row of pixels represents a world map with the larger pixels at the top of the figure representing the map at the greatest distance (95 m) from the imager. The linear grayscale represents the intensity seen in a pixel normalized to the maximum counts (black) in the entire image. The source is clearly visible at center of the top row of pixels of the image. The distance of closest approach was 95 m. The distance to the source is primarily determined from the change in parallax as the data in the different distance-of-closest-approach detector arrays are mapped to the corresponding world-pixel maps.

2) Simulation Results: The code was used to optimize the imager with restrictions placed on the parameters as follows. First, the pixel and mask sizes were fixed to the size of the existing detector elements. Second, a focal length of one meter was used to keep the pixel size at 100 m below 10 m and to limit the size of the unit. Finally, a mask thickness of 4 cm was used to provide attenuation of the radiation out to several MeV.

We first ran a series of simulations to select the best imager length. This is determined by the number of pixels in the image. The results are shown in Fig. 7 where we plot the detected (maximum) signal versus the distance of closest approach to the source and the number of pixels in the image. The later is varied by changing both the number of mask and detector

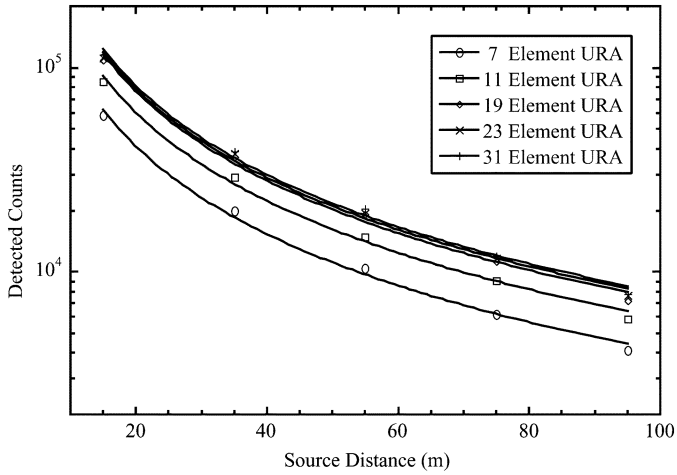

Fig. 7. Detected counts versus source distance of closest approach for different fields of view as represented by the number of pixels in the image. The curves for the largest three images are almost coincident. Note that to limit statistical noise, a simulated source strength of 10 mCi was used.

pixels while holding the total detector area fixed by changing the pixel height. As one adds pixels, the field of view of the imager increases so that a source is in the field of view for a longer period of time. (Full collimation to one cycle of the mask pattern was used in the simulations, see below). As can be seen, the advantage gained from more pixels diminishes as the field of view is increased beyond ~ 45 degrees. At large angles, the projected detector area and the long range to the source mean that few events are obtained and only small increases in sensitivity will occur for imagers larger then 19 pixels. These results were found to hold down to the lowest energy lines of interest at ~ 100 keV, indicating that atmospheric absorption did not significantly limit the performance at wide fields of view.

In imaging objects at a finite distance, one must include the geometric projection effects that magnify the mask pattern at the detector [5]. A source at a distance of closest approach, b, will magnify the mask pixel, a, by a factor

$$\frac{a'}{a} = \frac{b+f}{b} \tag{3}$$

where f is the distance between the mask and the detector. Magnification factors differing from one by a few percent can cause artifacts in the decoded image. Although these are mostly washed out as a source transits through the field of view in a scan, there is a net loss in efficiency since contrast in the shadow pattern is lost. Ideally, one would use detectors without mechanically defined (fixed) pixel sizes (as was done in the simulation with the 10 different detector arrays each representing different binning of the same data.) As this was not possible here, we chose to optimize the system for distant sources and matched the mask pattern pitch to the detector pitch. This sacrifices some of the sensitivity to nearby sources, however, these sources are already the most detectable because of the higher count rate. A second set of simulations was used to determine whether collimation was needed. For a normal imager the mask is made of two repetitions of the base pattern and has twice the number of pixels as the detector. Images of objects that walk out of one side of the field of view will wrap or suddenly appear on the other

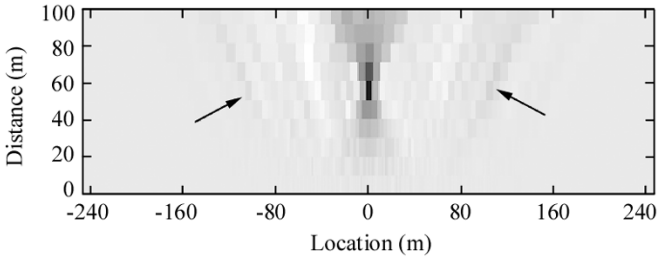

Fig. 8. Scan with no background showing the ghost peaks before and after the main source (at arrows). The data represents a 1 mCi source at 55 m closest approach for a 1 m^2 detector traveling at 40 km/hr.

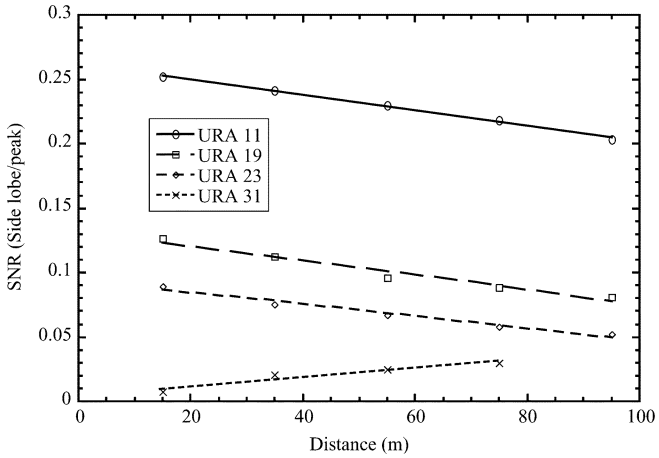

Fig. 9. Size of the ghost peak due to the lack of collimation as a fraction of the main peak height for different numbers of mask (and corresponding detector) elements.

side of the image as the source continues to move out of the field of view. This is a result of partial mask patterns projected by the source onto the detector and is of concern in our test imager. One solution to this problem is to restrict the field of view of a single detector pixel to one cycle of the mask pattern (19 pixels) by using slat collimators between the pixels. (This was used in the length optimization described above.) However, the collimators reduce the flux from the source as it transits the field of view and also add weight and complexity to the imager. Simulations with no collimation beyond that inherent in the 4-cm mask thickness were run. The results (Fig. 8) show that a strong point source will have a weak ghost peak before and after the main peak. The size of the peak varies with the number of mask elements as shown in Fig. 9. The small side peaks of our 19-element coded aperture were not considered worth suppressing because of the loss in sensitivity that would result from additional collimation.

An additional complication posed by the use of the existing detectors was the large individual pixel size. Ideally, to avoid aliasing effects, one oversamples the mask pattern using a detector pixel-pitch half that of the mask pixel-pitch [11]. This would mean mask pixels of the order of 20 cm, leading to an unwieldy focal length for the desired $\sim$10 m pixel size at the maximum range. In addition, a coded aperture pattern of 19 pixels means a 38-pixel mask that would be almost 8 meters long, requiring an unrealistically long vehicle. The 4 meter length of the

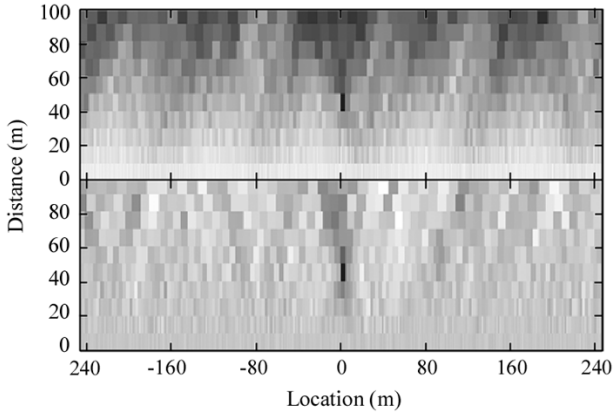

Fig. 10. Scan past a 0.5 mCi source at 45 m, with 500 cnts/m^2/sec sinusoidal modulation on a background of 1 000 cnts/m^2/sec. In the upper scan, a single pass is made at 35 km/h with a one square meter detector. In the lower panel two passes are made each with a 0.5 m^2 detector. One scan is made using the mask, the other with an "anti-mask". The two pass approach clearly removes the sinusoidal background. (A residual of the pattern is slightly visible due to the varying counting statistics where the background is higher.)

mask with the one-to-one sampling we use is another reason to desire smaller detector pixels.

A technique that significantly enhances the robustness of coded aperture imaging is the use of sequential, equal-time, mask and anti-mask acquisitions. By interchanging open and closed elements of the mask pattern, one can remove spurious variations in counts versus position in the detector [12]. Such variations are inevitably present and lead to artifacts in the image. In the scanning system described here, use of this technique is problematic. A second option, to simultaneously obtain the data with two vertically stacked systems was considered. Due to the different radiation environments of imagers placed one above the other, a serial approach was deemed better. Unfortunately, following a mask imager by an anti-mask imager would result in an unacceptably long instrument (8 m) due to the fixed detector pixel size. As this is a proof-of-principle instrument for the imaging technique, we opted to take separate scans past the same source field, once with the mask pattern and a second time with its inverse. To effect the change, a number of mask elements are rotated about axes of anti-symmetry, while others are raised or lowered into or out of the detector field of view.

The advantage of the mask/anti-mask technique is shown graphically in Fig. 10 where we impose a leakage background (unmodulated by the mask) that varies sinusiodally with detector position. The varying background that dominates the system response in the mask-only data, shows only as increased statistical noise in the mask/anti-mask decoded image.

B. Mechanical Design

Based on the results of the simulations, an instrument using a one-dimensional, 19-element-base, coded-aperture pattern was constructed. The mask elements are made of linotype metal. This provides almost the density of lead but is structurally superior. The mask elements are 75 cm high to provide a vertical field of view designed to cover a two-story building at 6 m and beyond. Their 4-cm thickness provides high contrast for gamma-ray energies up to 3 MeV. The elements are captured

in a steel frame as shown in Fig. 4. The system can be rapidly reconfigured from mask to the anti-mask configuration.

The detectors are mounted to a plate that is held in a similar, although smaller, frame. Each of the 19 pixels is comprised of three of the $10 \times 10 \times 10$ cm^3 detectors stacked vertically. To protect the NaI(Tl) detectors from thermal shock, the instrument is mounted in the rear of a temperature-controlled truck.

C. Electronics

A custom 64-channel data acquisition system (one channel for each scintillator-photomultiplier (PMT) detector) has been constructed to handle data from the system. The PMT's are operated at a nominal gain of 10^5. The event-generated charge from a PMT is converted into a voltage by a local capacitor connected directly to the anode at the PMT base. A voltage amplifier also connected to the PMT anode, sends the signal to the processing electronics.

The pulse processing system is built around a gated integrator with a parallel fast channel. A discriminator in the fast channel recognizes an event and initiates the signal processing cycle in the gated integrator. Voltage signals from a PMT are converted back into a short charge pulse and integrated for 2.2 μs. The integrated signal is then converted by a low-power, 16-bit ADC and decimated to an 11-bit word. This provides near-nuclear quality conversion without the use of dithering.

Every ADC generates an interrupt signal when it has valid data. The interrupt signals are decoded by a priority encoder and serviced by the steering logic. The ADC data is combined with the PMT number to form an event word. This is stored in a FIFO buffer. To allow a world-image map to be generated, the logic also generates periodic time-stamp events and imager-location events (the latter, through decoding of data from a fifth wheel attached to the vehicle.) These are also stored in the FIFO buffer. A fast PCI interface (National Instruments PCI-6534) [13] is used to perform high-speed data transfer between the electronics and a personal computer.

The system is designed to withstand a sustained rate of $\sim$100 kcps per channel. Total power consumption for the data acquisition system is $\sim$75 W. It is designed to run off of the vehicle power supply. Several tests have been performed and the system shows resolution performance dominated by the detector statistics.

III. Preliminary Performance

To verify the imaging performance of the system, we have performed stationary tests using one row of detectors and a very early version of the acquisition system (originally constructed for a 19×19 Ge strip detector) [14].

In preparation for the tests, the gains of the detectors were approximately equalized by varying the gain of the photomultiplier tubes. Residual gain variations were removed by an automated fitting routine that performed a chi-square minimization to Gaussian line profiles of data collected using a ^{137}Cs and a ^{60}Co source.

The calibrated imager was used with a shortened focal length of 36 cm. This allows the use of weaker sources at closer range, while maintaining the pixel sizes. A first image of a point source is shown in Fig. 11. The background where the images were collected is unremarkable. The source was placed 10 meters from the mask with the imager sitting just inside the roll-up door of a high bay of a metal sided building. The source was located outside on asphalt pavement while the imager itself sat on the concrete pad of the building.

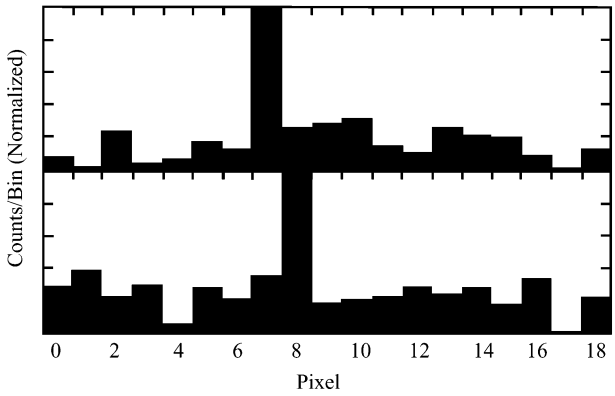

Fig. 11. Two images of a 30 μCi source at 10 meters taken in one second with one third of the final detector area. The source is moved by one pixel between the two images.

IV. Conclusion

Preliminary results from the instrument indicate that it performs as expected. The sensitivity to stationary point sources matches simulation results. Further tests are planned with the detector driven past fixed sources once the full electronics system is completed. In addition, the system will be used to measure the spatially varying and directional nature of the natural and man-made radiation environment.

Acknowledgment

The authors would like to thank the mechanical engineering support provided by T. Decker, the mechanical design and development work of D. Carter and D. Carr, and the contributions of summer students J. McDonald and E. Alexander, all with the Lawrence Livermore National Laboratory. The authors would also like to thank J.-F. Beche at Lawrence Berkeley National Laboratory for his work on the data acquisition system.

References

[1] K. Ziock and W. Goldstein, "The lost source, varying backgrounds and why bigger may not be better," in *Proc. Conf. Unattended Radiation Sensor Systems for Remote Applications, AIP*, vol. 632, J. Trombka, D. Spears, and P. Solomon, Eds., 2002, pp. 60–70.

[2] N. N. Jibiri, "Assessment of health risk levels associated with terrestrial gamma radiation dose rates in Nigeria," *Environ. Int.*, vol. 27, pp. 21–26, 2001.

[3] A. C. Paul *et al.*, "Population exposure to airborne thorium at the high natural radiation areas in India," *J. Environ. Radioactivity*, vol. 40, pp. 251–259, 1998.

[4] A. S. Mollah *et al.*, "Measurement of high natural background radiation levels by TLD at Cox's bazar coastal areas in Bangladesh," *Radiat. Protection Dosimetry*, vol. 18, pp. 39–41, 1987.

[5] E. E. Fenimore and T. M. Cannon, "Coded aperture imaging with uniformly redundant arrays," *Appl. Opticsi.*, vol. 17, no. 3, pp. 337–347, Feb. 1978.

[6] G. J. Hurford, E. J. Schmahl, R. A. Schwartz, A. J. Conway, M. J. Aschwanden, A. Csillaghy, B. R. Dennis, C. Johns-Krull, S. Krucker, R. P. Lin, J. Mctiernan, T. R. Metcalf, J. Sato, and D. M. Smith, "The RHESSI imaging concept," *Sol. Phys.*, vol. 210, pp. 61–86, 2002.

[7] T. A. Prince and G. J. Hurford, "Gamma-ray and hard X-ray imaging of solar flares," *Sol. Phys.*, vol. 118, pp. 269–290, 1988.

[8] E. E. Fenimore, "Coded aperture imaging: Predicted performance of uniformly redundant arrays," *Appl. Opt.*, vol. 17, no. 22, pp. 3562–3570, Nov. 1978.

[9] S. Gottesman and E. Fenimore, "New family of binary arrays for coded aperture imaging," *Appl. Opt.*, vol. 28, no. 20, pp. 4344–4352, Oct. 1989.

[10] W. Press, S. Teukolsky, W. Vetterling, and B. Flannery, *Numerical Recipes in C*. New York: Cambridge Univ. Press, 1995, p. 294.

[11] E. Caroli, J. Stephen, G. di Cocco, L. Natalucci, and A. Spizzichino, "Coded aperture imaging in X- and gamma-ray astronomy," *Space Sci. Rev.*, vol. 45, no. 3–4, pp. 349–403, Jan. 1987.

[12] C. Brown, "Multiplex imaging with multiple-pinhole cameras," *J. Appl. Phys.*, vol. 45, no. 4, pp. 1806–1811, Apr. 1974.

[13] National Instruments (2004). [Online]. Available: http://www.ni.com/

[14] K. Ziock, N. Madden, E. Hull, W. Craig, T. Lavietes, and C. Cork, "A germanium-based coded aperture imager," *IEEE Trans. Nucl. Sci.*, vol. 49, no. 4, pp. 1737–1742, Aug. 2002.